JOURNAL OF THE AMERICAN CHEMICAL SOCIETY

Article

Reversible and Persistent Electrical Bistability in Single Crystals of a Self-Assembled π-Conjugated Tetraaryl System: A Submicrometer Scale Electrical Characterization

Shay Tal, Batya Blumer-Ganon, Moshe Kapon, and Yoav Eichen

J. Am. Chem. Soc., **2005**, 127 (27), 9848-9854• DOI: 10.1021/ja051154n • Publication Date (Web): 16 June 2005

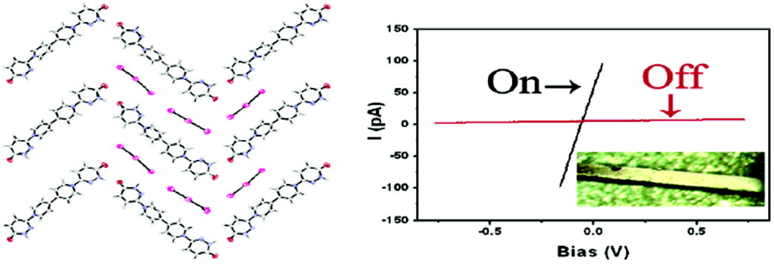

ACS Publications
High quality. High impact.

Journal of the American Chemical Society is published by the American Chemical Society. 1155 Sixteenth Street N.W., Washington, DC 20036

J|A|C|S
ARTICLES

Reversible and Persistent Electrical Bistability in Single Crystals of a Self-Assembled π-Conjugated Tetraaryl System: A Submicrometer Scale Electrical Characterization

Shay Tal,[†] Batya Blumer-Ganon,[†] Moshe Kapon,[†] and Yoav Eichen*,[†,‡]

Contribution from the Department of Chemistry and Solid State Institute, Technion − Israel Institute of Technology, Technion City, 32000, Haifa, Israel

Received February 23, 2005; E-mail: chryoav@techunix.technion.ac.il

Abstract: A new π-conjugated electroactive 4,4′-bipyridinium that bears two pyridazone self-complementary units was prepared and characterized. The new system readily assembles and forms at least two stable charge-transfer crystalline structures having a thermal population of unpaired electrons. The crystals of one phase exhibit electrical bistability, displaying either high (ON) and low (OFF) conductivity, at the same applied bias, depending on the electrical history of the system. The relation between the supramolecular structure of the crystals and their electrical properties is also discussed.

I. Introduction

Since the discovery of organic semiconductors, immense efforts have been directed toward their application as active electronic media in different electronic components such as light emitting diodes,[1] transistors,[2] solar cells,[3,4] capacitors,[5] miniaturized circuitry,[6] and so forth.[7,8] The inherent richness of the organic realm offers some unique possibilities in using organic semiconductors in new fields, such as sensing of organic target molecules, in which inorganic microelectronic is very limited.[9−11]

The main attraction of organic semiconductors arises from the fact that they can be tailor-made to specific specifications and that there is an infinite number of possible combinations to such systems. Another major advantage is that, unlike the collective nature of the electronic properties of inorganic materials, the basic electronic properties are of molecular character. This presents the possibility of using individual molecules or small numbers of them as building blocks for organic electronic components and circuits.[12]

Recent publications report on certain conjugated organic devices that exhibit current−voltage (I−V) characteristics that depend on the voltage sweep direction, implying the presence of two conducting states of the organic semiconductor.[13−19] A number of mechanisms have been proposed to account for the existence of these states and the switching between them. The low conductivity state (OFF state) is attributed to the presence of deep traps for charge carriers in the organic medium. These traps lead to low carrier mobility and high resistance. Under high fields the traps become occupied, leading to high carrier mobility (ON state) and low resistance of the organic medium. The electrical bistability originates from the high electrical fields that are required to access or change the occupancy of the traps.

Another mechanism for electrical bistability of organic devices that was suggested in recent years involves the voltage-induced modulation of the width of the depletion region.[13] Decreasing the width of that layer to below the tunneling limit generates the highly conductive state (ON state), while increasing the width of that layer to beyond the tunneling limit is responsible for the formation of the low-conductivity state (OFF state).

Recently, such electrical bistability of organic semiconductors has been explained in terms of electrochemical processes that lead to changes in the electronic properties of the molecules.[17,18] Similar systems that are based on electrooptical read/write mechanisms were also reported. In such systems, charges are

---

[†] Department of Chemistry.

[‡] Solid State Institute.

(1) Friend, R. H.; Gymer, R. W.; Holmes, A. B.; Burroughes, J. H.; Marks, R. N.; Taliani, C.; Bradley, D. D. C.; Dos Santos, D. A.; Bredas, J. L.; Logdlund, M.; Salaneck, W. R. *Nature* **1999**, *397*, 121−128.

(2) Wurthner, F. *Angew. Chem., Int. Ed.* **2001**, *40*, 1037−1039.

(3) Hagfeldt, A.; Graetzel, M. *Acc. Chem. Res.* **2000**, *33*, 269−277.

(4) Woehrle, D.; Meissner, D. *Adv. Mater.* **1991**, *3*, 129−138.

(5) Min, G. *Synth. Met.* **2003**, *135−136*, 141−143.

(6) Rogers, J. A.; Bao, Z.; Meier, M.; Dodabalapur, A.; Schueller, O. J. A.; Whitesides, G. M. *Synth. Met.* **2000**, *115*, 5−11.

(7) Tsutsui, T.; Fujita, K. *Adv. Mater.* **2002**, *14*, 949−952.

(8) MacDiarmid, A. G. *Angew. Chem., Int. Ed.* **2001**, *40*, 2581−2590.

(9) Aviram, A.; Ratner, M. A. *Chem. Phys. Lett.* **1974**, *29*, 277−283.

(10) Mujica, V.; Kemp, M.; Roitberg, A.; Ratner, M. *J. Chem. Phys.* **1996**, *104*, 7296−7305.

(11) Carroll, R. L.; Gorman, C. B. *Angew. Chem., Int. Ed.* **2002**, *41*, 4378−4400.

(12) Ellenbogen, J. C.; Love, J. C. *Proc. IEEE* **2000**, *88*, 386−426.

(13) Taylor, D. M.; Mills, C. A. *J. Appl. Phys.* **2001**, *90*, 306−309.

(14) Smith, S.; Forrest, S. R. *Appl. Phys. Lett.* **2004**, *84*, 5019−5021.

(15) Majumdar, H. S.; Bandyopadhyay, A.; Bolognesi, A.; Pal, A. J. *J. Appl. Phys.* **2002**, *91*, 2433−2437.

(16) Bandyopadhyay, A.; Pal, A. J. *Adv. Mater.* **2003**, *15*, 1949−1952.

(17) Moller, S.; Forrest, S. R.; Perlov, C.; Jackson, W.; Taussig, C. *J. Appl. Phys.* **2003**, *94*, 7811−7819.

(18) Moller, S.; Perlov, C.; Jackson, W.; Taussig, C.; Forrest, S. R. *Nature* **2003**, *426*, 166−169.

(19) Mushrush, M.; Facchetti, A.; Lefenfeld, M.; Katz, H. E.; Marks, T. J. *J. Am. Chem. Soc.* **2003**, *125*, 9414−9423.

(20) (a) Liu, C.; Pan, H.; Fox, M. A.; Bard, A. J. *Chem. Mater.* **1997**, *9*, 1422−1429. (b) Fox, M. A.; Grant, J. V.; Melamed, D.; Torimoto, T.; Liu, C.; Bard, A. J. *Chem. Mater.* **1998**, *10*, 1771−1776. (c) Gregg, B. A.; Fox, M. A.; Bard, A. J. *J. Phys. Chem.* **1989**, *93*, 4221−4234. (d) Liu, C.; Pan, H.; Tang, H.; Fox, M. A.; Bard, A. J. *J. Phys. Chem.* **1995**, *99*, 7632−7636. (e) Liu, C.; Pan, H.; Fox, M. A.; Bard, A. J. *Science* **1993**, *261*, 897−899.

10.1021/ja051154n CCC: $30.25

trapped in a liquid crystalline medium. The release of the trapped charges may be switched ON and OFF by an optical signal.[20]

Devices that exhibit electrical bistability may be suitable for data-storage applications. In such devices, one can "write" information using high electrical fields (high voltage), "read" it many times by applying a small probe voltage, and "erase" the stored data using high electrical fields of the opposite direction. Nevertheless, there is a need to deepen the understanding of the structure−electrical activity correlation in such systems because of the lack of simple guidelines for the preparation and selection of effective and reversible electrically bistable systems. The use of crystalline systems offers both very flat and well-defined writing surfaces as well as a well-defined structure of the electroactive system.

Here we report on the preparation and characterization of a new π-conjugated electroactive 4,4′-bipyridinium that bears two pyridazone self-complementary units. The new system readily assembles and forms at least two stable charge-transfer crystalline structures having a thermal population of unpaired electrons.

The crystals of one phase exhibit electrical bistability, displaying either high (ON) or low (OFF) conductivity, at the same applied bias, depending on the electrical history of the system. The reversible and persistent electrical bistability that is found in one crystalline phase of the self-assembled π-conjugated tetraaryl system is studied using an atomic force microscope equipped with a conductive tip. The correlation between the supramolecular structure of the crystal and the electrical properties is also discussed.

II. Experimental Section

II.a. Apparatus. NMR spectra were recorded on a Bruker AC-200F spectrometer. Mass spectra were recorded using a triple quadruple TSQ-70 Spectrometer (Finnigan MAT). Melting points were recorded on a PL-DSC (Polymer Laboratories) machine. Electrochemical measurements were performed on a computer-controlled AUTOLAB PGSTAT12 potentiostat equipped with a three-compartment cell having a platinum counter electrode and a Ag/AgNO$_3$ reference electrode (silver wire in a solution of 0.01 M AgNO$_3$ in dry acetonitrile). The reference electrode was calibrated against *N*,*N*′-dimethyl-4,4′-bipyridinium (−0.768 and −1.227 V versus Ag/AgNO$_3$ reference electrode in acetonitrile).[21] A platinum wire electrode was used as the working electrode for all the electrochemical measurements, and an ITO-coated glass electrode was used for all the spectroelectrochemical measurements. All measurements were performed in dry and deoxygenated acetonitrile solutions containing 0.1 M tetrabutylammonium hexafluorophosphate as the electrolyte. All the electrochemical redox data are given as (Epa + Epc)/2.

Spectroelectrochemistry data were collected at fixed applied potentials using a computer-controlled diode array spectrometer (SM240, CVI) that was optically coupled to the electrochemical cell using fiber optics.

EPR spectra were recorded on a Bruker EMX-10/12 X-band ($\upsilon = 9.4$ GHz) digital EPR spectrometer. All spectra were recorded at a nonsaturating microwave power 2.0 mW, 100 kHz magnetic field modulation of 1.0 G amplitude. The digital field resolution was 2048 points per spectrum. Spectra processing and simulation were performed with Bruker WIN-EPR Software.

SPM electrical and topographic characterization of the two crystalline phases of $\mathbf{1}^{2+}\bullet\mathbf{2I_3}^-$ was performed using an atomic force microscope, AFM (Digital Instruments, Dimension 3100), equipped with a conductive tip (MESP tips, NANOPROBE) in the TUNA (Tunneling AFM) and topographic modes. The crystals were mounted on a gold-coated glass holder, using silver paste (see Figures 5b and 6b). The electrical AFM measurements were performed at a scan rate of 0.1 Hz.

II.b. Materials. *N*,*N*′-Bis-(6-oxo-1,6-dihydro-pyridazin-3-yl)-4,4′-pyridinium, $\mathbf{1}^{2+}$: Route A: A 10:1 mixture of 3,6-dichloropyridazine and 4,4′-bipyridine was heated to 120 °C under an inert atmosphere for 2 days. The crude was chromatographed (silica, 5 g L^{-1} ammonium chloride in a 2:3 water/methanol solution). The fractions of the eluent that contained the product were combined and concentrated under reduced pressure. The product was precipitated from the concentrated solution by adding a concentrated solution of ammonium hexafluorophosphate. The resulting precipitate, *N*,*N*′-(3,3′-di-(6-chloropyridazine))-4,4′-bipyridinium bis-hexafluorophosphate, $\mathbf{2}^{2+}\bullet\mathbf{2PF_6}^-$, was obtained in 80% yield. The dichloride salt $\mathbf{2}^{2+}\bullet\mathbf{2Cl}^-$ was obtained by adding a saturated acetone solution of $\mathbf{2}^{2+}\bullet\mathbf{2PF_6}^-$ to an acetone solution of tetrabutylammonium chloride. NMR, MS, and crystal structure data for $\mathbf{2}^{2+}\bullet\mathbf{2PF_6}^-$ and $\mathbf{2}^{2+}\bullet\mathbf{2Cl}^-$ are provided in the Supporting Information. Treating $\mathbf{2}^{2+}\bullet\mathbf{2Cl}^-$ with an aqueous solution of potassium iodide yielded *N*,*N*′-bis-(6-oxo-1,6-dihydro-pyridazin-3-yl)-4,4′-pyridinium bis-triiodide, $\mathbf{1}^{2+}\bullet\mathbf{2I_3}^-$ as a dark powder with a metallic luster.

Route B: A 10:1 mixture of 3-chloro-6-hydroxy pyridazine and 4,4′-bipyridine was heated to 140 °C under inert atmosphere for 7 days. The crude was chromatographed (silica, 5 g L^{-1} ammonium chloride in a 2:3 water/methanol solution), and the fractions of the eluent that contained the product were concentrated under reduced pressure. The product was precipitated from the concentrated solution by adding to it a concentrated solution of ammonium hexafluorophosphate. The precipitate, *N*,*N*′-bis-(6-oxo-1,6-dihydro-pyridazin-3-yl)-4,4′-pyridinium bis-hexafluorophosphate, $\mathbf{1}^{2+}\bullet\mathbf{2PF_6}^-$, was obtained in 52% yield.

^{1}H NMR (DMSO-d_6): δ ppm 9.73 (4H, d), 9.06 (4H, d), 8.26 (2H, d), 7.3 (2H, d); ^{13}C NMR (DMSO-d_6): δ ppm 160.25, 143.69, 132.4, 129.26, 126.76.

II.c. Crystallography. Single crystals of $\mathbf{1}^{2+}\bullet\mathbf{2I_3}^-$**-A** and $\mathbf{1}^{2+}\bullet\mathbf{2I_3}^-$**-B** of dimensions 0.33 × 0.09 × 0.06 mm^3 and 0.30 × 0.30 × 0.01 mm^3, respectively, were mounted on a KappaCCD diffractometer, and the data were collected using Mo Kα radiation. Intensities were collected at 298 (2) K using ω and φ scans and processed using the "Collect" data collection software[22] and DENZO-SMN for cell refinement and data reduction.[23] The structures were solved by direct methods using the "maXus"[24] package and refined using SHELXL-97.[25] SHELXL-97 was also used for material publication. ORTEP and TEXRAY were used for structure analysis.[26]

All the non-hydrogen atoms of $\mathbf{1}^{2+}\bullet\mathbf{2I_3}^-$**-A** were refined anisotropically. The hydrogen atoms were then placed at their calculated positions, and refined isotropically by applying the riding model. Structure $\mathbf{1}^{2+}\bullet\mathbf{2I_3}^-$**-B** was refined anisotropically with respect to the half organic dication and triiodide anion and isotropically with respect to the hydrogen atoms by applying the riding model. The difference Fourier maps of $\mathbf{1}^{2+}\bullet\mathbf{2I_3}^-$**-B** revealed numerous peaks of low electron density, ascribed to water molecules occupying in a disordered way the rectangular cavities formed by the ions. Twenty eight such positions with a variety of occupancies were introduced into the model and refined isotropically until convergence was reached.

III. Results and Discussion

III.a. Synthesis. The two different approaches that were applied to the preparation of *N*,*N*′-bis-(6-oxo-1,6-dihydro-

---

(21) Bird, C. L.; Kuhn, A. T. *Chem. Soc. Rev.* **1981**, *10*, 49−82.

(22) Nonius, KappaCCD Server Software; Nonius BV: Delft, The Netherlands, 1997.

(23) Otwinowski, Z.; Minor, W. *Methods Enzymol.* **1997**, *276*, 307−326.

(24) Mackay, S.; Gilmore, C. J.; Edwards, C.; Tremayne, M.; Stuart, N.; Shankland, K. "maXus", a computer program for the solution and refinement of crystal structures from diffraction data; University of Glasgow: Scotland, U.K., Nonius BV, Delft: The Netherlands, and MacScience Co. Ltd.: Yokohama, Japan, 1998.

(25) Sheldrick, G. M. *SHELXL97*, program for the refinement of crystal structures; University of Göttingen: Göttingen, Germany, 1997.

(26) *ORTEP*, TEXRAY Structure Analysis Package; Molecular Structure Corporation: The Woodlands, TX, 1999.

Scheme 1 [a]

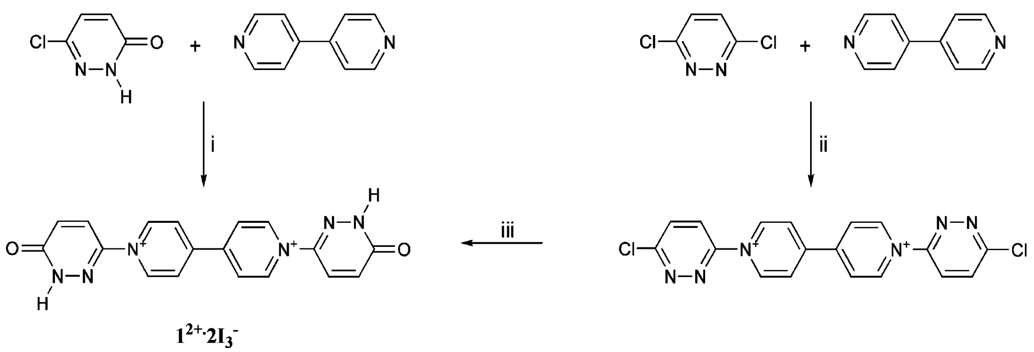

[a] (i) 140 °C, 7d, Ar, 52% yield. (ii) 120 °C, 2d, Ar, 80% yield. (iii) Saturated aqueous KI solution, quant.

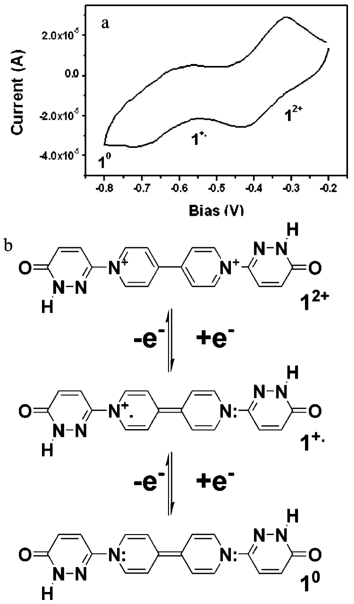

Figure 1. (a) Cyclic voltammogram of **1** in acetonitrile. Electrolyte = 1×10^{-2} M $N(Bu)_4{}^+PF_6{}^-$; scan rate = 3 V s^{-1}; reference electrode = $Ag/AgNO_3$; working and counter electrodes = Pt. (b) Schematic presentation of the redox cycle of **1**.

pyridazin-3-yl)-4,4′-pyridinium, $\mathbf{1}^{2+}$, are depicted in Scheme 1. Heating a 10:1 mixture of 3-chloro-6-hydroxy pyridazine and 4,4′-bipyridine to 140 °C under inert atmosphere for 7 days produced a mixture of the mono- and bisalkylated bipyridinium together with a small quantity of the starting material.

In an alternative route, a 10:1 mixture of 3,6-dichloropyridazine and 4,4′-bipyridine was heated to 120 °C under an inert atmosphere for 2 days, then the (3,3′-di-(6-chloropyridazine))-4,4′-bipyridinium was isolated by column chromatography. Treatment of the (3,3′-di-(6-chloropyridazine))-4,4′-bipyridinium with an aqueous solution of potassium iodide yields *N*,*N*′-bis-(6-oxo-1,6-dihydro-pyridazin-3-yl)-4,4′-pyridinium bis triiodide, $\mathbf{1}^{2+}\bullet\mathbf{2I_3}^-$, as the sole product.

II.b. Electrochemical and Spectroelectrochemical Characterization. Similar to most bipyridinium salts, $\mathbf{1}^{2+}$ is electroactive, showing relatively mild reduction potentials of $E_{2+\rightarrow 1+} = -0.379$ and $E_{1+\rightarrow 0} = -0.64$ V versus $Ag/AgNO_3$ (+0.16 and −0.10 V versus NHE) at a scan rate of 3 V s^{-1} (Figure 1). The cyclic voltammogram is found to depend strongly on the scan rate. At high scan rates (>3 V s^{-1}) two symmetrical redox waves exist, characteristics of a doubly reducible system.

Upon decreasing the scan rate, we found that the oxidation peak of the doubly reduced species disappears while the oxidation of the singly reduced species is increased, an indication of a disproportionation reaction (eq 1) where V^0, $V^{+\bullet}$, and V^{2+} denote the doubly reduced, singly reduced, and nonreduced states of **1**, respectively.[27]

$$V^0 + V^{2+} \rightleftarrows 2V^{+\bullet} \qquad (1)$$

This behavior is a well-documented characteristic of bibyridinium salts that strongly interact with one another.[21] The singly and doubly reduced states are characterized by progressively red-shifted UV−vis absorption spectra. The high and low energy peaks shift from $\lambda = 292$ and 359 nm in the nonreduced form, $\mathbf{1}^{2+}$, through $\lambda = 455$, 700, and 725 nm in the monoreduced state, $\mathbf{1}^{+\bullet}$, to $\lambda = 560$ and >800 nm in the doubly reduced state, $\mathbf{1}^{\mathbf{0}}$. This progressive red-shift indicates the increased contribution of extended conjugation of the system in the reduced states.

III.c. Crystal Structures. Crystals of $\mathbf{1}^{2+}\bullet\mathbf{2I_3}^-$ were obtained by placing saturated aqueous solutions of $\mathbf{2}^{2+}\bullet\mathbf{2Cl}^-$ and potassium iodide into two compartments that were separated by a cellulose membrane. The crystals first grew atop the cellulose membrane than in the compartment of the organic material. Two different phases of $\mathbf{1}^{2+}\bullet\mathbf{2I_3}^-$ were identified in the vessel: one monoclinic, $P2_1/n$, denoted $\mathbf{1}^{2+}\bullet\mathbf{2I_3}^-$**-A** (Figure 2a−c), and the other orthorhombic, *Pccn*, denoted $\mathbf{1}^{2+}\bullet\mathbf{2I_3}^-$**-B** (Figure 3a−c).

Phase $\mathbf{1}^{2+}\bullet\mathbf{2I_3}^-$-A. Crystals of $\mathbf{1}^{2+}\bullet\mathbf{2I_3}^-$**-A** were obtained in the form of long needles and are characterized by a metallic luster. The crystal structure of $\mathbf{1}^{2+}\bullet\mathbf{2I_3}^-$**-A** is made up of layers each containing organic dications and triiodide anions extending parallel to the *bc* plane (Figure 2a). Each layer consists of herringbone-type ribbons of the organic dications separated by zigzag triiodide chains extending on the average along the *b* axis. The two dications are hydrogen-bonded through a N−H group of one ion and an O═C group of its neighbor, $d_{O(26)\cdots N(3)} = 2.784$ Å. The four six-membered rings of the dication are not coplanar. The interplanar angles between each two adjacent rings are $\theta_{ring(C2-C7)-ring(N8-C13)} = 29.8°$, $\theta_{ring(N8-C13)-ring(C14-C19)} = 26.2°$, and $\theta_{ring(C14-C19)-ring(C20-C25)} = 37.8°$. The two triiodide counterions are not symmetric and are slightly bent. These ions interact along the zigzag chain, giving rise to two nonbonded interactions $d_{I(1)\cdots I(4)} = 3.914$ Å and $d_{I(3)\cdots I(6)} = 3.983$ Å. The weaker interaction occurs when the triiodide ions approach approximately along the ion axis and becomes stronger when the approach is ca. 90° to this axis. The two triiodide anions

---

(27) See Supporting Information.

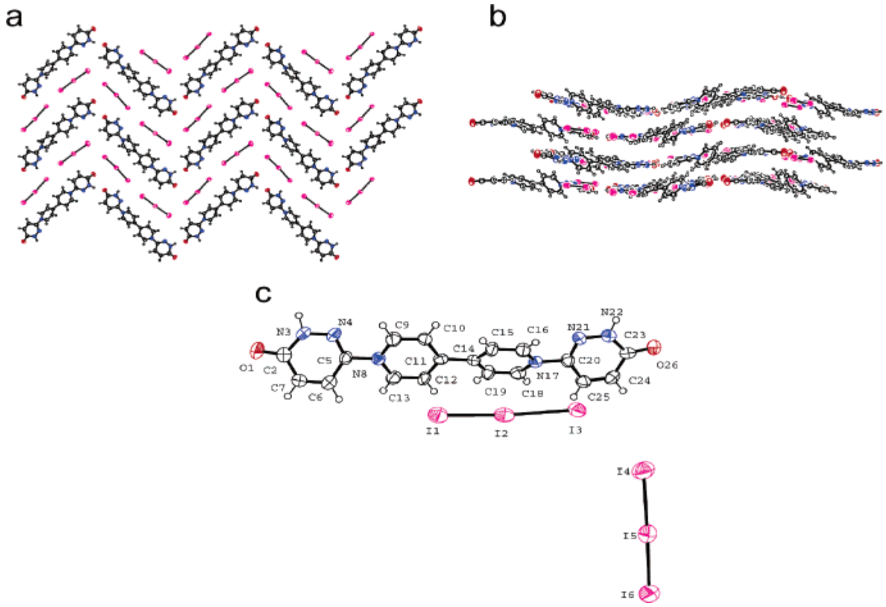

Figure 2. View of the crystal structure of $\mathbf{1^{2+}{\bullet}2I_3^{-}}$**-A**. (a) A layer containing organic dications and triiodide anions extending parallel to the bc plane. (b) The packing motif of several layers. (c) Atom numbering for $\mathbf{1^{2+}{\bullet}2I_3^{-}}$**-A**.

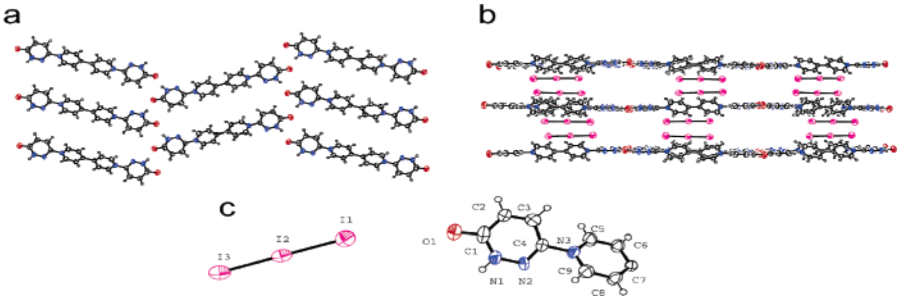

Figure 3. View of the crystal structure of $\mathbf{1^{2+}{\bullet}2I_3^{-}}$**-B**. (a) A layer containing the organic dications extending parallel to the *bc* plane. (b) The packing motif of several layers. (c) Atom numbering for $\mathbf{1^{2+}{\bullet}2I_3^{-}}$**-B**.

are characterized by slightly different geometry, $d_{I(1)\cdots I(2)} = 2.817$ Å, $d_{I(2)\cdots I(3)} = 3.126$ Å, $\alpha_{I(1)\cdots I(2)\cdots I(3)} = 174.86°$, and $d_{I(4)\cdots I(5)} = 2.983$ Å, $d_{I(5)\cdots I(6)} = 2.870$ Å, $\alpha_{I(4)\cdots I(5)\cdots I(6)} = 178.28°$. A strong hydrogen bond between the first triiodide and its neighboring pyridazone, $d_{I(3)\cdots N(22)} = 3.563$ Å, and a strong non-hydrogen bonding interaction between the second triiodide and its neighboring pyridazone, $d_{I(5)\cdots N(4)} = 3.614$ Å, are found to interconnect the organic herringbone-type ribbons and the zigzag chains.

Phase $\mathbf{1^{2+}{\bullet}2I_3^{-}}$-B. Crystals of phase $\mathbf{1^{2+}{\bullet}2I_3^{-}}$**-B** were obtained in the form of small rectangular dark plates. The crystal structure of $\mathbf{1^{2+}{\bullet}2I_3^{-}}$**-B** consists of neat layers of organic dications extending parallel to the *bc* plane (Figure 3a) and triiodide ions parallel to these layers, extending along the *c* axis. Both organic layers and triiodide ions form the walls of a rectangular channels extending along the *c* axis. These channels are occupied by water molecules in a disordered fashion. Twenty eight such sites with a variety of occupancies were found. The organic layer consists of herringbone-type ribbons of dications extending on the average along the *b* axis.

The ions are held together by hydrogen bonds involving the terminal N−H and C═O groups on each ion. Each terminal H−N−C═O group makes two symmetry-related hydrogen bonds $d_{O(1)\cdots N(1)} = 2.768$ Å with two neighboring organic cations. The cation resides on an inversion center with the outer rings being not coplanar with their neighboring pyridazone rings.

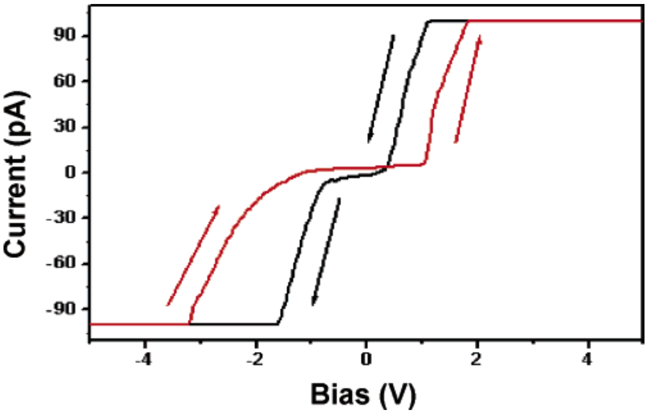

Figure 4. TUNA-generated *I*−*V* curves of $\mathbf{1^{2+}{\bullet}2I_3^{-}}$**-A** in the two scanning directions. Red line: scanning from −5 to +5 V, and black line: scanning from +5 to −5 V. Scan rate = 2 V s^{-1}. Bottom contact = silver. TUNA tip = MESP(Si).

The interplanar angle between pyridinium and pyridazone rings is $\theta_{\mathrm{ring(C1-N1)-ring(N3-C9)}} = 41.5°$. The pyridinium rings, through the inversion center, are coplanar. Contrary to the situation in the first crystal structure, $\mathbf{1^{2+}{\bullet}2I_3^{-}}$**-A**, the parallel triiodide anions do not interact strongly with one another but only through normal van der Waals forces. The triiodide ions are almost symmetric and linear: $d_{I(1)\cdots I(2)} = 2.971$ Å, $d_{I(2)\cdots I(3)} = 2.873$ Å, $\alpha_{I(1)\cdots I(2)\cdots I(3)} = 179.18°$. Here too, short contacts are

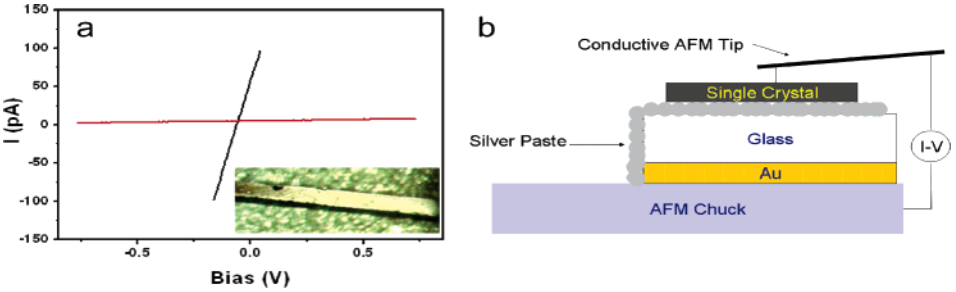

Figure 5. (a) TUNA-generated *I*−*V* curves of one point on the crystal of phase $\mathbf{1^{2+}{\bullet}2I_3^-}$**-A** in the range of −0.75 to +0.75 V, after applying −5 V erasing signal (red) and after applying +5 V writing signal (black). Scan rate = 2 V s^{-1}. Bottom contact = silver. TUNA tip = MESP (Si). (b) Scheme of the experimental setup. Inset: Picture of the inspected crystal on a silver contact.

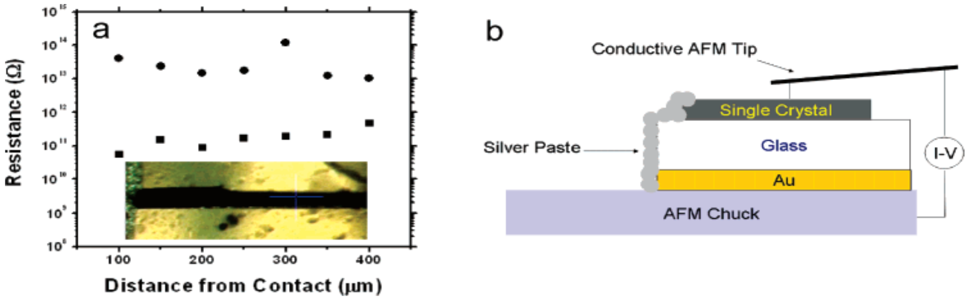

Figure 6. (a) Resistance of a crystal of phase $\mathbf{1^{2+}{\bullet}2I_3^-}$**-A** as a function of the distance from the contact for the "ON" state (■) and for the "OFF" state (●). Scan rate = 2 V s^{-1}. Bottom contact = silver. TUNA tip = MESP (Si). (b) Scheme of the experimental setup. Inset: Picture of crystal sticking out of the silver contact.

found between the dications and triiodides $d_{\mathrm{I(1)\cdots N(3)}} = 3.758$ Å and $d_{\mathrm{I(3)\cdots N(3)}} = 3.758$ Å.

The two crystalline phases of $\mathbf{1^{2+}{\bullet}2I_3^-}$ are ESR-active, indicating the presence of thermally accessible electronic state with unpaired electrons, presumably a charge-transfer state.[28−30]

III.d. AFM Electrical Characterization. Two terminal electrical measurements were made on a long, needlelike crystal sticking out of a conductive silver paste, as shown in Figure 5b, using AFM in the TUNA mode.

The resultant *I*−*V* curves are highly nonlinear and asymmetric with respect to zero bias. The shape of the curves depends on the voltage scan direction (indicated by arrows in Figure 4). Starting from a large positive bias, the curve is almost ohmic. Approaching zero voltage from large positive bias, a low-current regime with a high differential resistance develops between 0.3 and −0.7 V. At larger negative bias the almost ohmic high current regime is regained. In contrast, starting from a large negative bias, the curve is clearly non-ohmic. Approaching zero voltage from a large negative bias, a low-current regime with a high differential resistance develops between −1.1 and +1.0 V. At larger positive bias, the curve is almost ohmic and the high current regime is regained. Repeated measurements of a given crystal, in the same scan direction, yield reproducible *I*−*V* curves.

The large and reproducible hysteresis that is found in the *I*−*V* curves in Figure 4 offers the opportunity to electrically "write" information onto the surface of the crystals using high positive bias, "read" it at low positive bias, and "erase" it with a high negative bias. Figure 5 displays the *I*−*V* curves of one point on the crystal of phase $\mathbf{1^{2+}{\bullet}2I_3^-}$**-A** in the range of −0.75 to +0.75 V, after applying −5 V (red, OFF erasing signal) and +5 V (ON writing signal) writing signals.[31]

As can be seen in the figure, the two curves exhibit ohmic behavior throughout the range of the applied bias of ±0.75 V, with a resistance in the order of 1 × 10^9 and 2.6 × 10^{11} Ω after applying the "write" ON and "erase" OFF signals, respectively. The signals that were stored on the surface of the crystals persisted for at least several hours and could be erased with no apparent electrical or physical damage to the surface of the crystal. This effect was reproduced on all the crystals of phase $\mathbf{1^{2+}{\bullet}2I_3^-}$**-A** that we have examined and in each spot along them, as can be seen in Figure 6. In contrast, the same experiments that were performed on the second crystalline phase $\mathbf{1^{2+}{\bullet}2I_3^-}$**-B** implied that this phase is an insulator, producing TUNA currents of less than 50 fA at ±12 V.

The "write" ON and "erase" OFF signals can be placed one next to the other in high density with no apparent diffusion and annihilation. Figure 7 presents two 1-μm-long and 0.125-μm-wide conductive and insulating bars that were placed side by side on the surface of the crystal using a conductive AFM tip. Figure 7a,b presents the writing process using +5 V for "writing" ON and −5 V for "erasing" OFF. Figure 7c,d presents the reading process using the same conductive AFM tip but applying only −0.1 V bias. The bars persisted for at least several hours and could be easily erased and rewritten simply by applying "writing ON" and "writing OFF" signals.

IV. Conclusions

A tetraaryl system, $\mathbf{1^{2+}}$, composed of a bipyridinium salt and two self-complementary pyridazone binding units was prepared and characterized. Tetraaryl $\mathbf{1^{2+}}$ forms two types of crystalline

---

(28) Yoshikawa, H.; Nishikiori, S.-I.; Ishida, T. *J. Phys. Chem. B* **2003**, *107*, 9261−9267.
(29) Kidowaki, M.; Tamaoki, N. *Chem. Commun.* **2003**, 290−291.
(30) Cooke, G.; Augier de Cremiers, H.; Duclairoir, F. M. A.; Gray, M.; Vaqueiro, P.; Powell, A. V.; Rosair, G.; Rotello, V. M. *Tetrahedron Lett.* **2001**, *42*, 5089−5091.

(31) All values are given with respect to the ground (stage chuck).

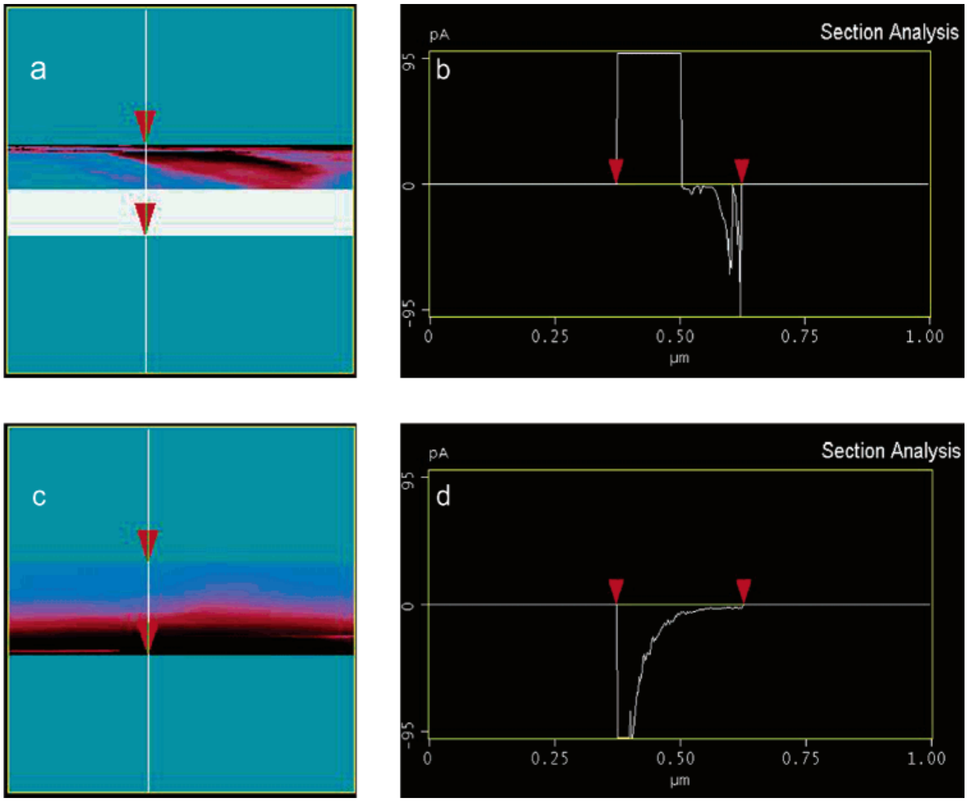

Figure 7. Two 1-μm-long and 0.125-μm-wide conductive and insulating bars that were recorded side by side on the surface of a crystal of $\mathbf{1^{2+}\bullet 2I_3^{-}}$**-A**. Signal bars were recorded by applying +5 V for "writing" ON and −5 V for "erasing" OFF and "reading" by applying −0.1 V, using a conductive AFM tip. Scan rate = 0.1 Hz. Bottom contact = silver. TUNA tip = MESP (Si). (a) TUNA image of the writing process. (b) Current-displacement cross section of (a). (c) TUNA image of the reading process. (d) Current-displacement cross section of (c).

phases of the triiodide salt, $\mathbf{1^{2+}\bullet 2I_3^{-}}$**-A** and $\mathbf{1^{2+}\bullet 2I_3^{-}}$**-B**. The two phases are ESR-active and are characterized by a dark color and indication of a charge−transfer crystal. Nevertheless, $\mathbf{1^{2+}\bullet 2I_3^{-}}$**-A** is characterized by semiconductor-type conductivity, while with $\mathbf{1^{2+}\bullet 2I_3^{-}}$**-B** we could not observe any conductivity. The two phases differ in two major structural properties: (a) phase $\mathbf{1^{2+}\bullet 2I_3^{-}}$**-A** is characterized by short inter-ionic distances between the I_3^- moieties. In contrast, the I_3^- groups in phase $\mathbf{1^{2+}\bullet 2I_3^{-}}$**-B** appear as isolated dimers that are separated from one another by solvent molecules and cationic species and (b) the two phases have rather similar arrangement of the cationic species parallel to the *bc* plane, meaning that they form two-dimensional layers of molecules that are interconnected via hydrogen bonds. Nevertheless, the two phases differ in the interaction between the two-dimensional layers, perpendicular to the *bc* plane. The layers of the cations in phase $\mathbf{1^{2+}\bullet 2I_3^{-}}$**-A** interact with each other perpendicular to the *bc* plane through rather short intermolecular $\pi-\pi$ interactions (mean interlayer distance of 3.595 Å). Since the alternating layers are shifted one with respect to the other, the cationic layers form a three-dimensional π-stacked assemblies. The layers of the cations in phase $\mathbf{1^{2+}\bullet 2I_3^{-}}$**-B** are separated by solvent molecules and triiodide dimers. Thus, the mean interlayer distance for the cationic species is 6.945 Å, a distance that does not offer any significant $\pi-\pi$ interactions. Correlating conductivity to structure, we find that the phase that is characterized by isolated cationic and anionic species is insulating. In contrast, the phase that is characterized by a three-dimensional tight packing of cationic species and zigzag chains of closely packed triiodide anions shows properties of a semiconductor. A comprehensive structure−conductivity study of a series of closely related bipyridinium derivatives is currently in process in our laboratory with the aim of better understanding the electrical behavior of such systems.

Two terminal electrical measurements on single crystals of $\mathbf{1^{2+}\bullet 2I_3^{-}}$**-A** using an atomic force microscope in the TUNA mode produce $I-V$ curves that are highly nonlinear and asymmetric with respect to zero bias. The large and reproducible hysteresis that is found in the $I-V$ curves offers the opportunity to electrically alter the electrical properties of the crystals, thus allowing us to "write" and "erase" conductive and insulating domains. The domains are space-localized and persistent, and due to the large hysteresis one can "read" their "write" or "erase" state using low bias. By applying +5 V (ON) and −5 V (OFF) signals to the surface of crystals of $\mathbf{1^{2+}\bullet 2I_3^{-}}$**-A**, we were able to alter the electrical response of the system by more than 3 orders of magnitude at short contact separation (100 μm). In contrast, $\mathbf{1^{2+}\bullet 2I_3^{-}}$**-B** was proved to be an insulator, producing TUNA currents of less than 50 fA at ±12 V. The ON and OFF signals could be "written" one next to the other in a rather high density with no apparent diffusion and annihilation, as was demonstrated by "writing" two adjacent 0.125 μm wide bars, one ON and one OFF.

The mechanism of the "writing" and "erasing" phenomena is not yet fully revealed. A rather high contact resistance is consistently being observed in each experiment. The contact resistance is found to be in the order of 1×10^{10} and 1×10^{13} Ω for the "write" (ON) and "erase" (OFF) processes, respectively. The differential resistance is also found to be different for the "write" (ON) and "erase" (OFF) processes, being in the range of 1 × 10^9 Ω/μm and higher than the capability of our measuring devices respectively for the ON and OFF states, respectively. The "write" process clearly decreases the contact resistance when compared to the "erase" process. This effect may arise from either filling surface charge traps that may exist on the surface of the crystal or from local electrochemistry that turns the contact zone into a better contact between the crystal and the tip of the AFM.

Owing to the highly asymmetric contact setup, we estimate that most, if not all, of the switching in the contact resistance originates from the tip to crystal interface. In such a case, the increase in conductivity is due to n-doping of the crystal. The same process could also account for the significant drop in bulk conductivity that is also observed in this system. Further study to reveal the nature of the ON/OFF processes is under way.

Acknowledgment. This joint research project was financially supported by the State of Lower Saxony and the Volkswagen-Stiftung (Grant No. I/79 461).

Supporting Information Available: Synthesis and characterization of $\mathbf{2^{2+}\bullet 2Cl^-}$ and $\mathbf{2^{2+}\bullet 2PF_6^-}$, cyclic voltammogram of **1** in different scan rates and crystallographic details for $\mathbf{1^{2+}\bullet 2I_3^-}$**-A** and $\mathbf{1^{2+}\bullet 2I_3^-}$**-B**. This material is available free of charge via the Internet at http://pubs.acs.org.

JA051154N